

https://dspace.org/

Aerodynamics of a spinning sphere: an investigation into the variation of lift and drag with velocity ratio and orientation of spin axis

Lewis, Russel Elliot

2011-02-23
http://hdl.handle.net/10539/9085

Downloaded from a DSpace repository. https://dspace.org/

6.2 VALIDATION OF CALIBRATION MATRIX

The validation consists of two sections. The first is a tare analysis. This section is not only to justify the assumption that the tare on a sting balance is negligible but also to see if there are any effects on the six components when the angle of yaw is changed, as this is the only angle being changed in this experiment.

The second section is the re-substitution of the calibration data into the calibration matrix to show where the errors are more serious.

6.2.1 TARE ANALYSIS

In this section the graphs of tare versus angle of yaw are given. The reason that only the yaw angle is considered is that the sphere was only tested with varying angle of yaw. This was done because the sphere required an angular change of 90^{o} and the limits in the attack direction were 30^{o}.

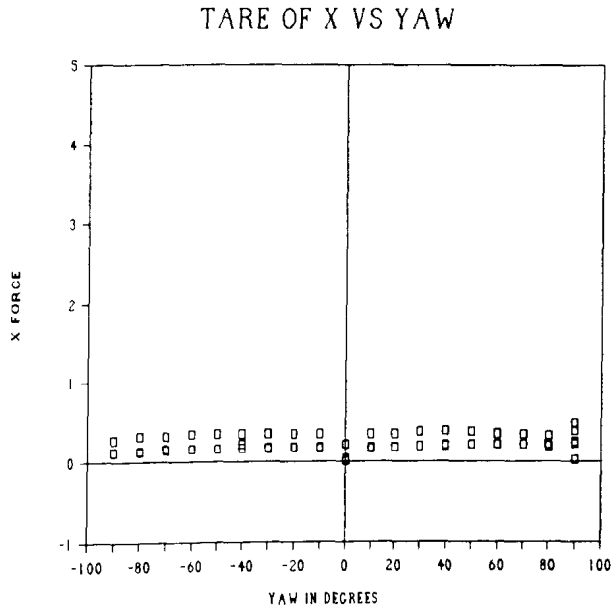


Fig. 6.1. Effect of wind loading on X component without a model in position 1.

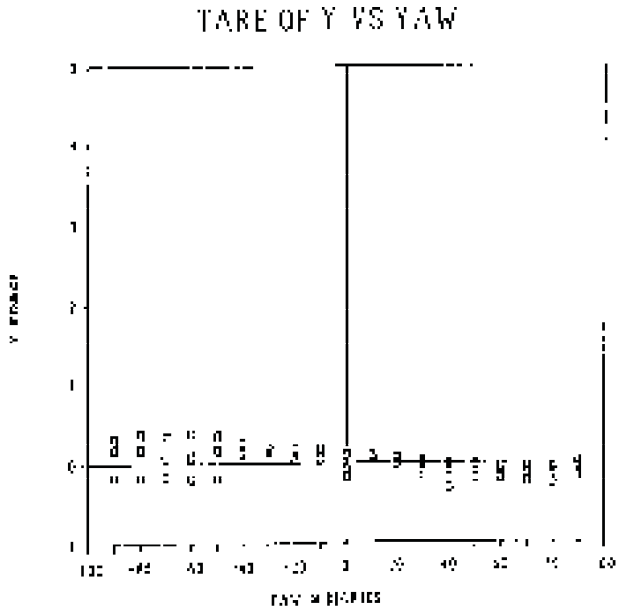


Fig. 6.2. Effect of wind loading on Y component without a model in position 1.

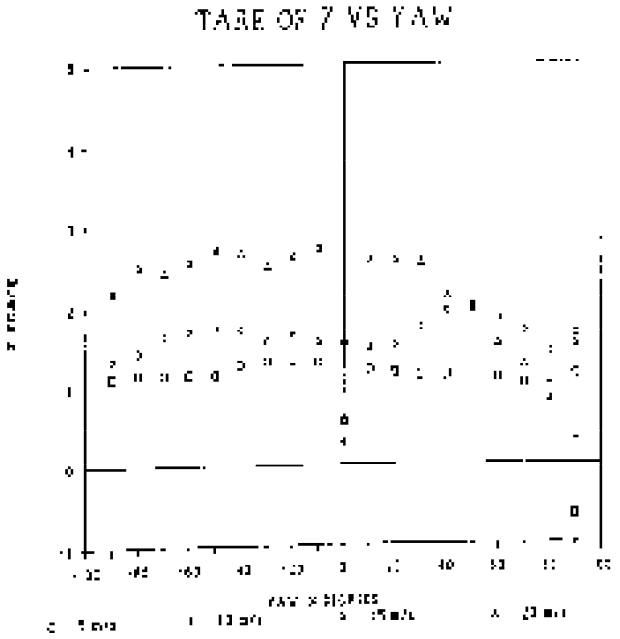


Fig. 6.3. Effect of wind loading on Z component without a model in position 1.

The tare effects on the forces were expected to be negligible since the virtual centre (centre of measurement) was so close to the end of the sting. An analogous system would be to place a set of transducers at the end of a cantilever and measure the loads applied closer to the fixed end. Since the tare on the Z component with respect to yaw was so high, a test was carried out of tare with respect to attack.

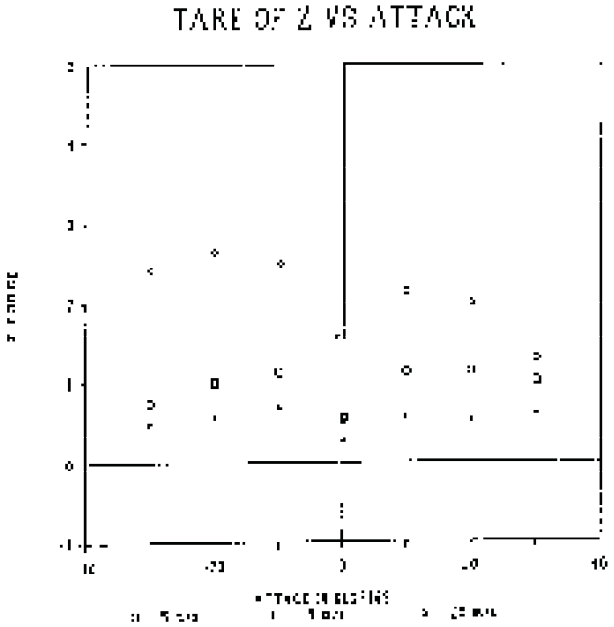


Fig. 6.4. Effect of wind loading on Z component without a model in position 1 with changing angle of attack.

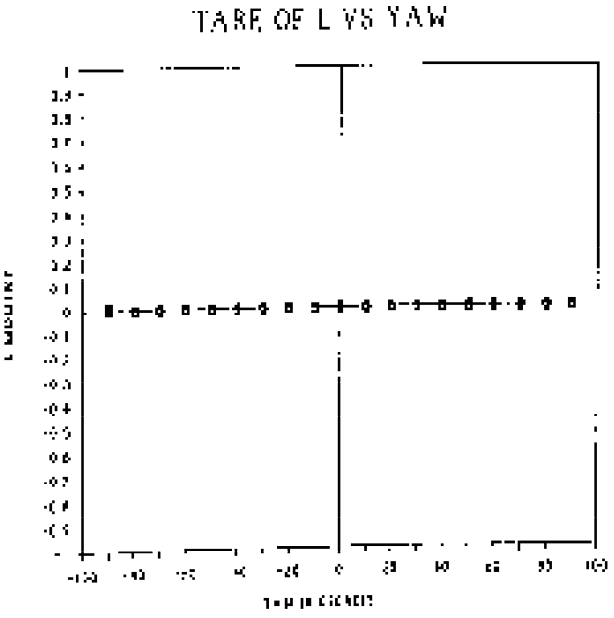


Fig. 6.5. Effect of wind loading on L component without a model in position 1.

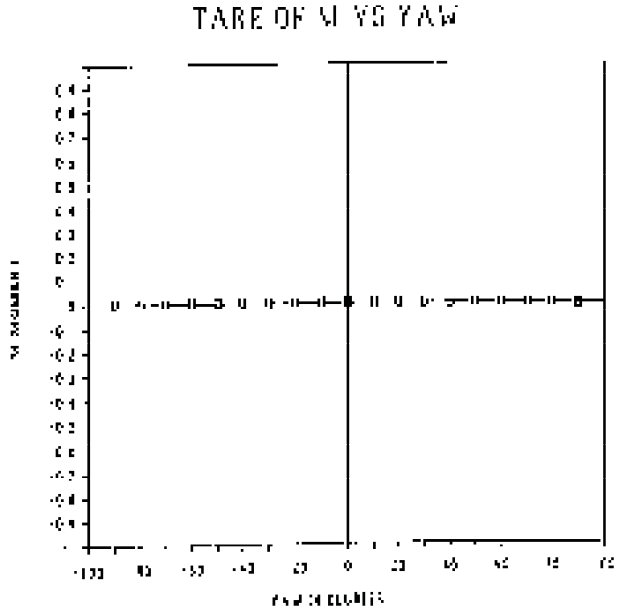


Fig. 6.6. **Effect of wind loading on M component without a model in position 1.**

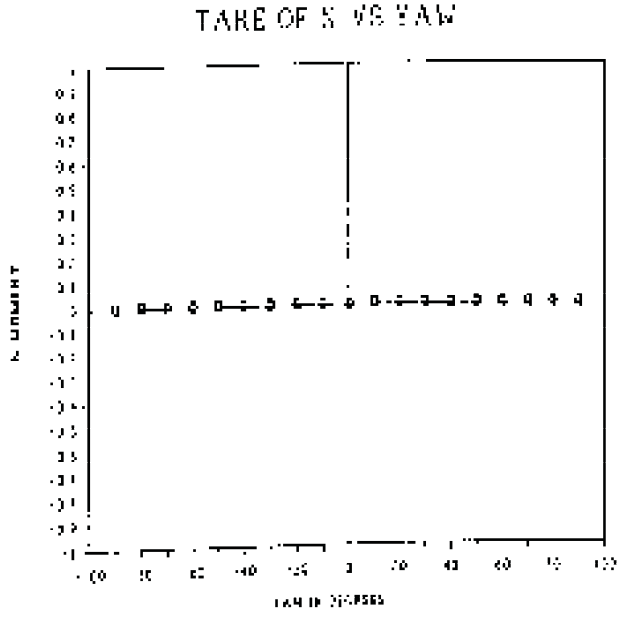


Fig. 6.7. **Effect of wind loading on N component without a model in position 1.**

The effects of tare on the moments measured were for all intents and purposes zero. This was to be expected since the virtual centre was so close to the end of the sting. This meant that any applied force was acting on a very small lever arm, resulting in an exceptionally small moment.

The tare tests were repeated after the sting was rotated through 90° and re-calibrated. The results of these tests are given below.

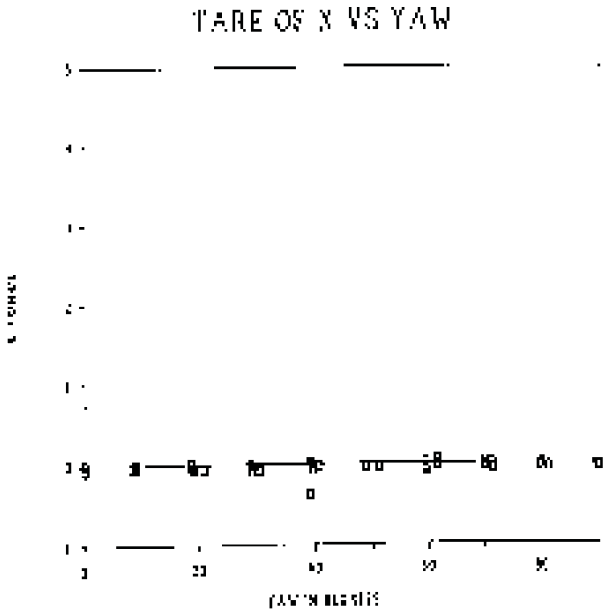


Fig. 6.8. Effect of wind loading on X component without a model in position 2.

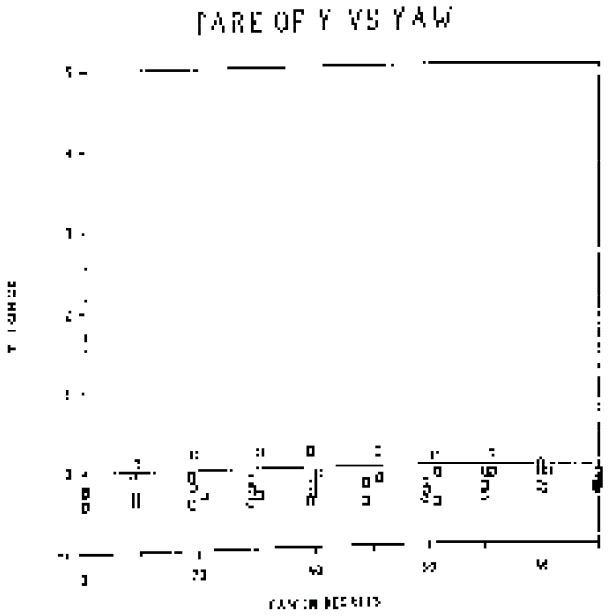


Fig. 6.9. Effect of wind loading on Y component without a model in position 2.

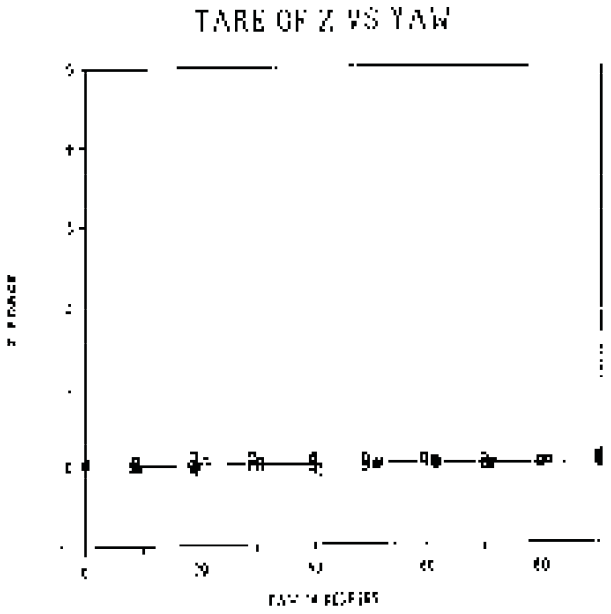


Fig. 6.10. Effect of wind loading on Z component without a model in position 2.

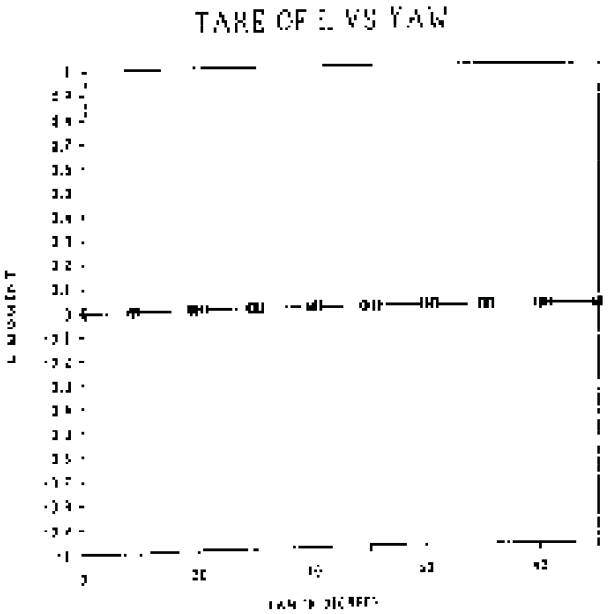


Fig. 6.11. Effect of wind loading on L component without a model in position 2.

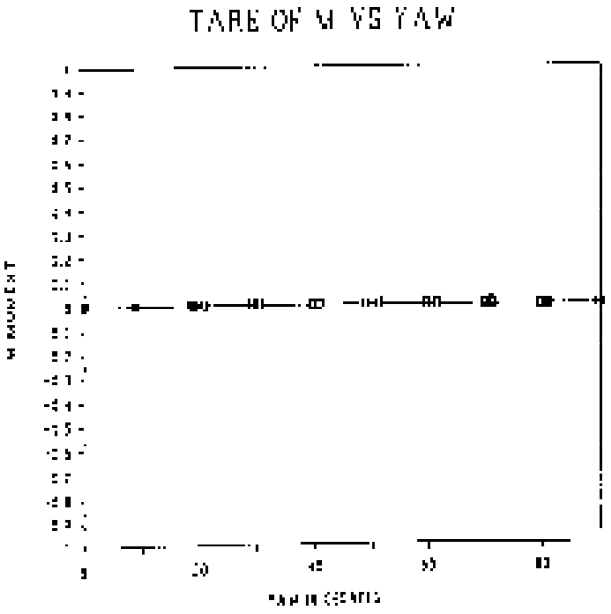


Fig. 6.12. Effect of wind loading on M component without a model in position 2.

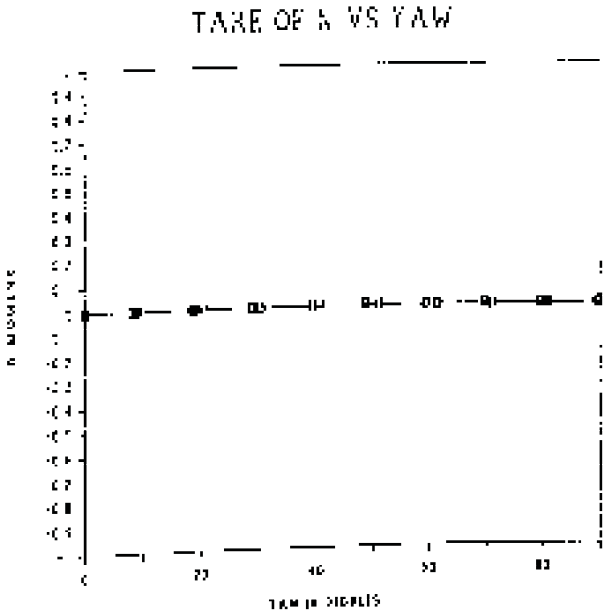


Fig. 6.13. Effect of wind loading on N component without a model in position 2.

6.2.2 CALIBRATION ANALYSIS

The validation of the calibration was carried out by re-substitution. The calibration data was then multiplied by the calibration matrix and the applied load compared to the measured load.

The following graphs show the applied load versus the measured load on each component. These loads include all the calibration tests.

The graph shows the measured load on each component for the sting being loaded in the X direction (increasing load and then decreasing load), then in the Y direction (increasing load and then decreasing load) with the point of application moving from station 1 to station 5 thereby changing the applied moment N, then the Z direction (increasing load and then decreasing load) with the point of application moving from station 1 to station 5 thereby changing the applied moment M, and finally in the Z direction with a displacement along the Y axis only, from station -3 to 3 with changing loads.

For schematic diagrams of the calibration stand, calibration body and loading jig see Appendix C figures 3.1, 3.2 and 3.3 respectively.

Once again the graphs for all three calibrations are shown. They appear in the same order as previously, first position 1 then position 2.

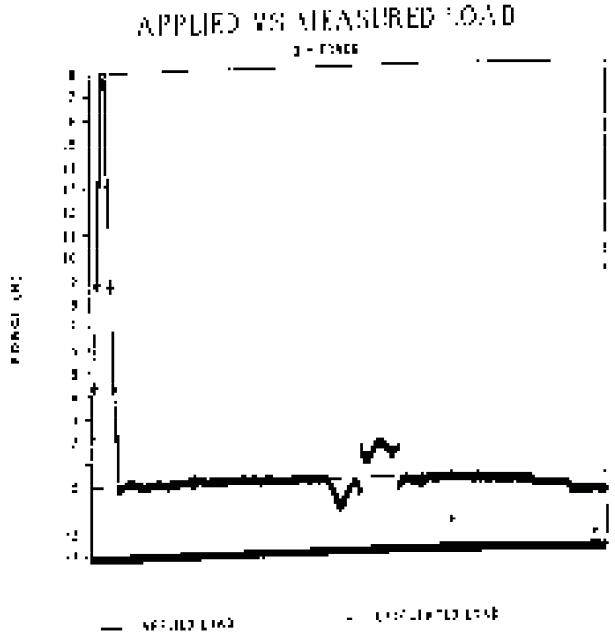


Fig. 6.14. Comparison of applied and calculated X force (position 1).

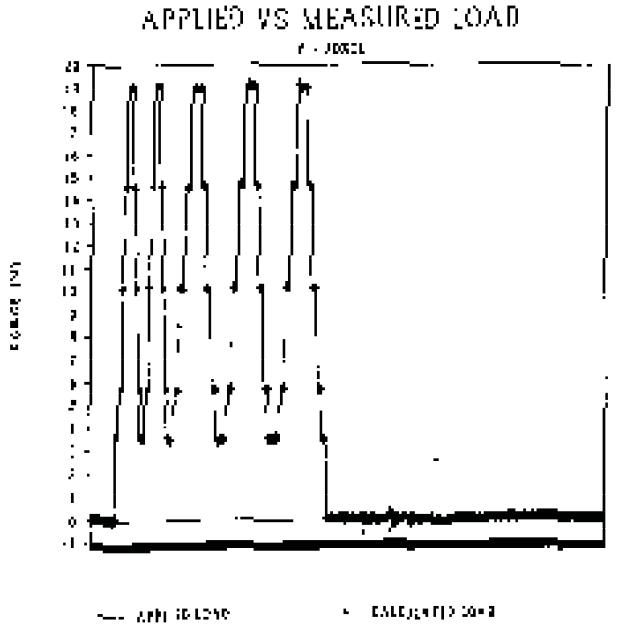


Fig. 6.15. Comparison of applied and calculated Y force (position 1).

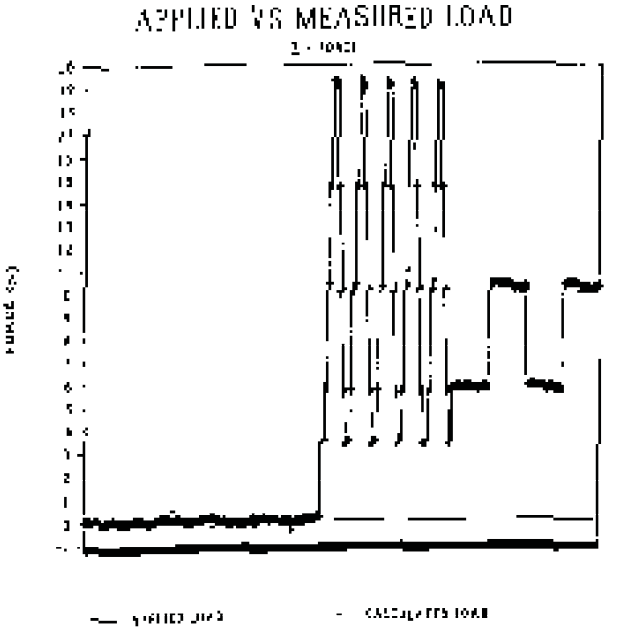


Fig. 6.16. Comparison of applied and calculated Z force (position 1).

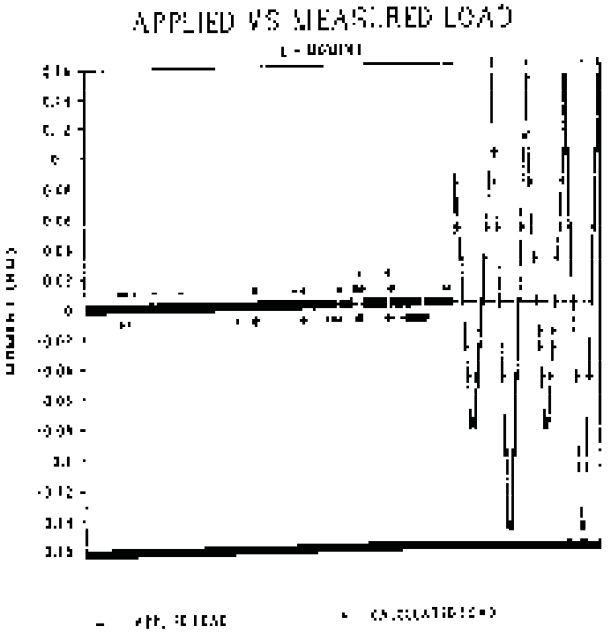


Fig. 6.17. Comparison of applied and calculated L moment (position 1).

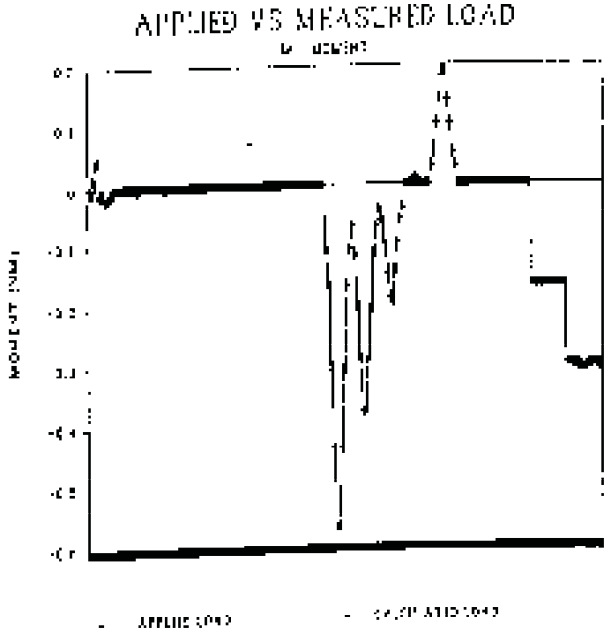


Fig. 6.18. Comparison of applied and calculated M moment (position 1).

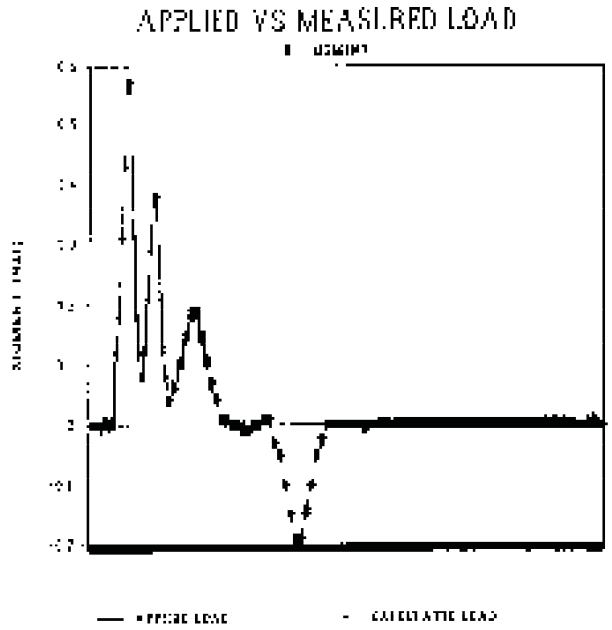


Fig. 6.19. Comparison of applied and calculated N moment (position 1).

The graphs below belong to the calibration which was carried out with the sting in position 2

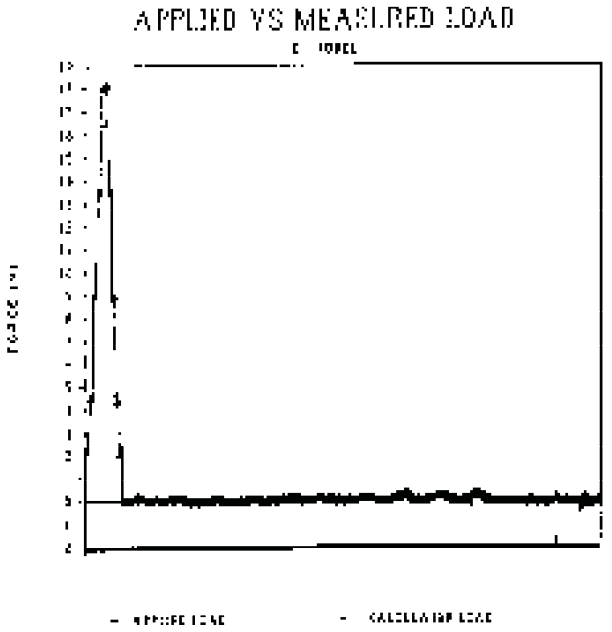


Fig. 6.20. Comparison of applied and calculated X force (position 2).

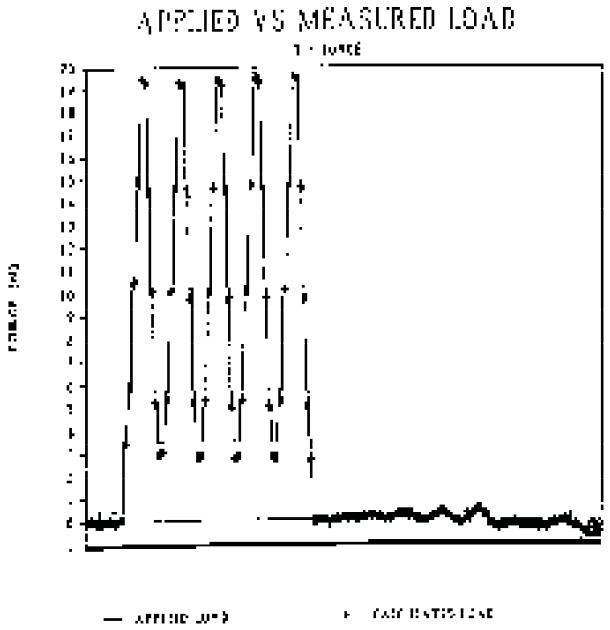


Fig. 6.21. Comparison of applied and calculated Y force (position 2).

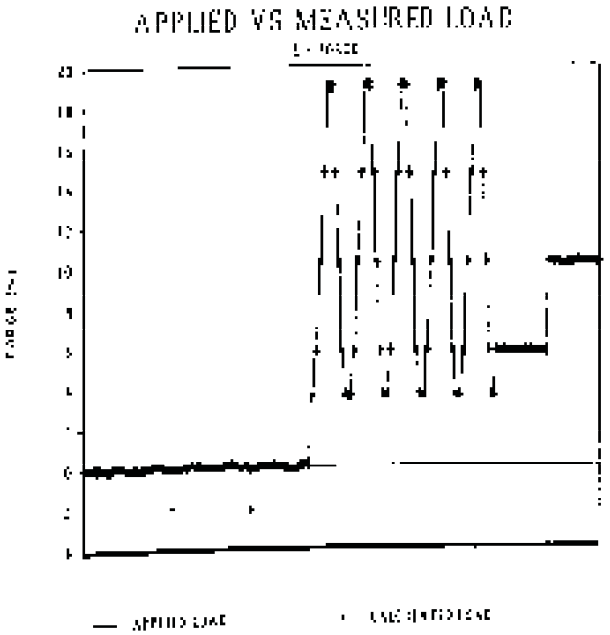


Fig. 6.22. Comparison of applied and calculated Z force (position 2).

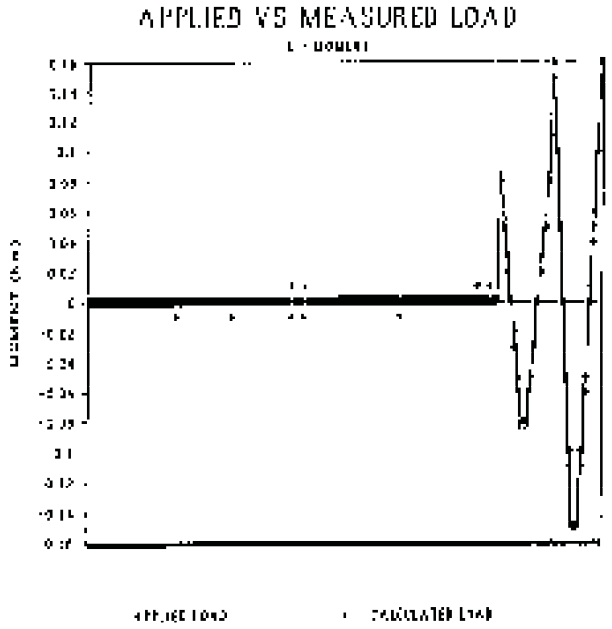


Fig. 6.23. Comparison of applied and calculated L moment (position 2).

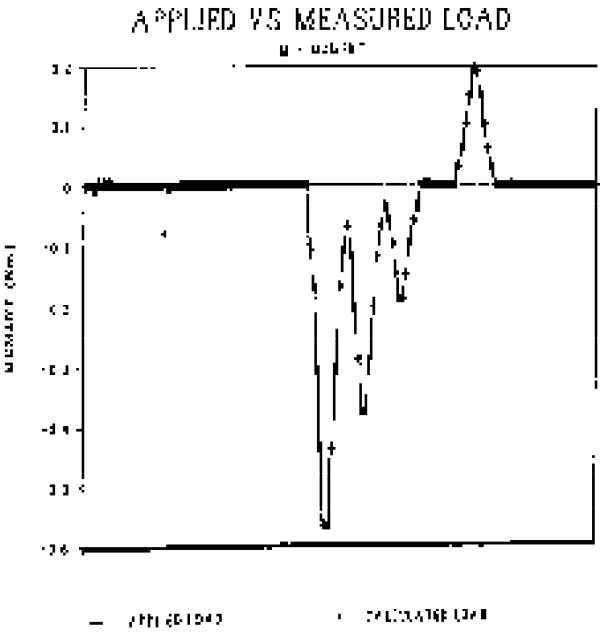


Fig. 6.24. Comparison of applied and calculated M moment (position 2).

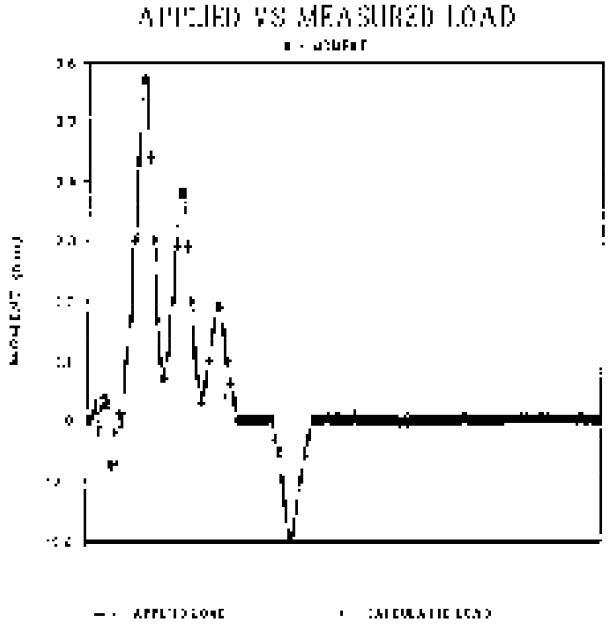


Fig. 6.25. Comparison of applied and calculated N moment (position 2).

It must be remembered that for each loading condition four readings were taken. From the above graphs it is evident that the data acquisition system did have a limited amount of random drift. This can be seen when the measured load shows one or two readings not having the same value as the applied load for that loading case.

What was more serious was cross linking that was not accounted for by the least squares curve fit. This was evident when looking at the deviation of the measured and applied loads in the graph of X force. This was due to some unaccounted for effect that the loading of a pitching moment has on the drag reading. The reverse effect was also evident since when the sting was loaded in the X direction there was a drift in the measured pitching moment. (See Fig. 10.24)

The other source of concern was the constant random drift on the channel measuring the rolling moment.

The only solution short of changing the data acquisition system is to take a large sample of data and either average out the readings or to use statistical methods to eliminate the stray points. The latter of these two is time consuming and would only warrant it if the degree of accuracy required it.

After the sting was repaired the same graphs were generated. These graphs are shown below.

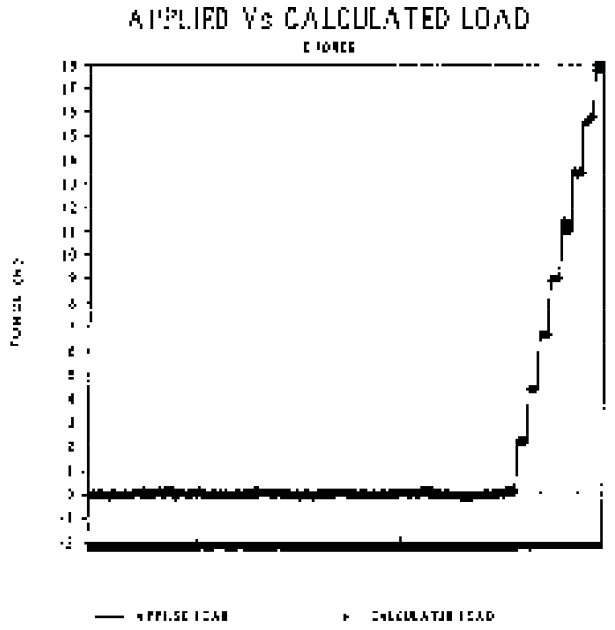


Fig. 6.26. Comparison of applied and calculated X force (position 2) after repair.

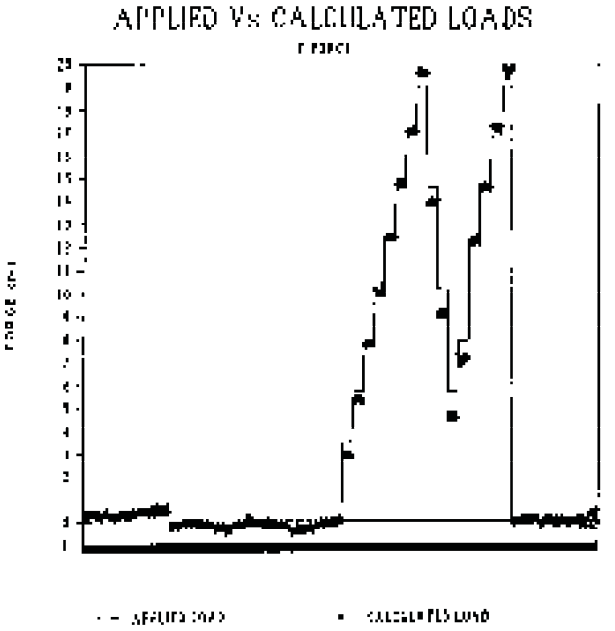


Fig. 6.27. Comparison of applied and calculated Y force (position 2) after repair.

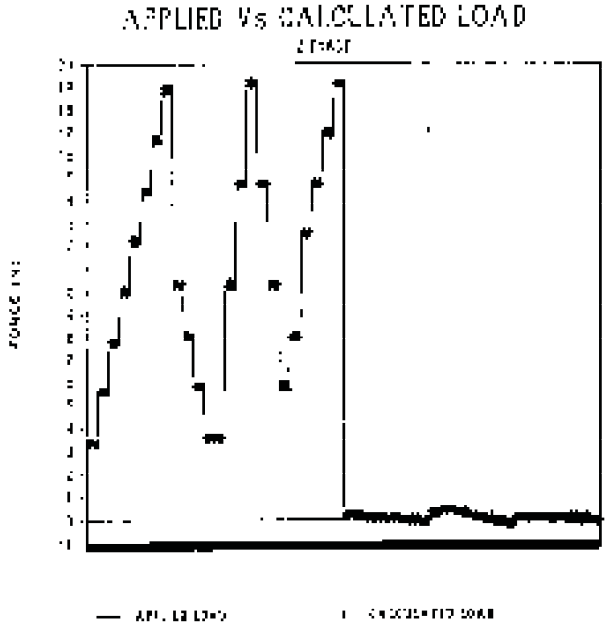


Fig. 6.28. Comparison of applied and calculated Z force (position 2) after repair.

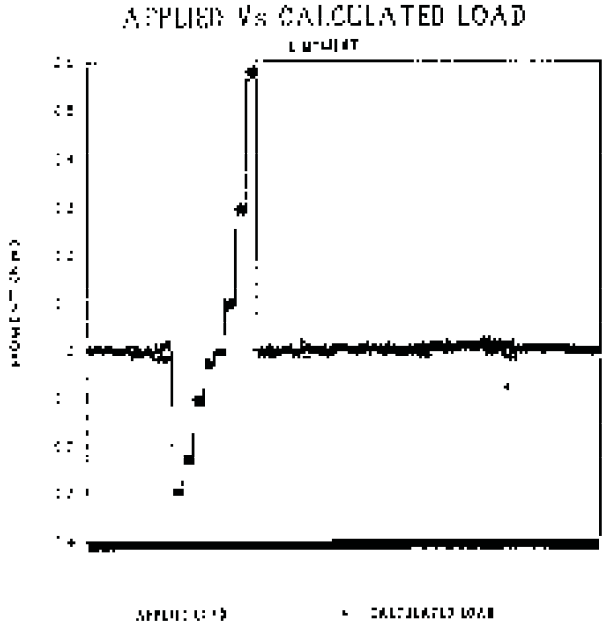


Fig. 6.29. Comparison of applied and calculated L moment after repair (position 2).

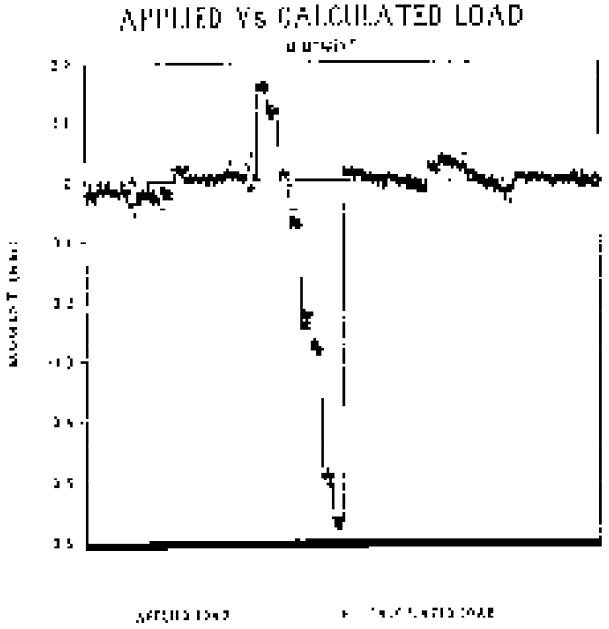


Fig. 6.30. Comparison of applied and calculated M moment after repair (position 2).

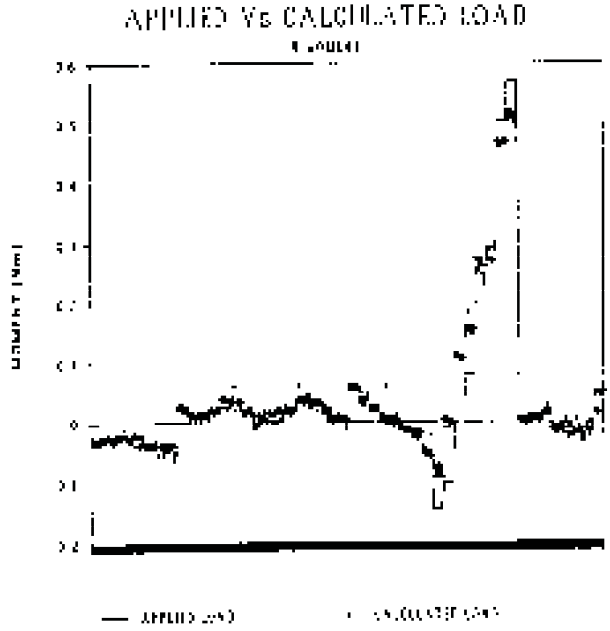


Fig. 6.31. Comparison of applied and calculated N moment after repair (position 2).

6.3 CALIBRATION OF THE ANGLE OF ATTACK AND YAW

The attack and yaw angles were calibrated by changing the angle and measuring the output. Linear regression was then carried out on these readings to give a linear relationship between the output and the angle.

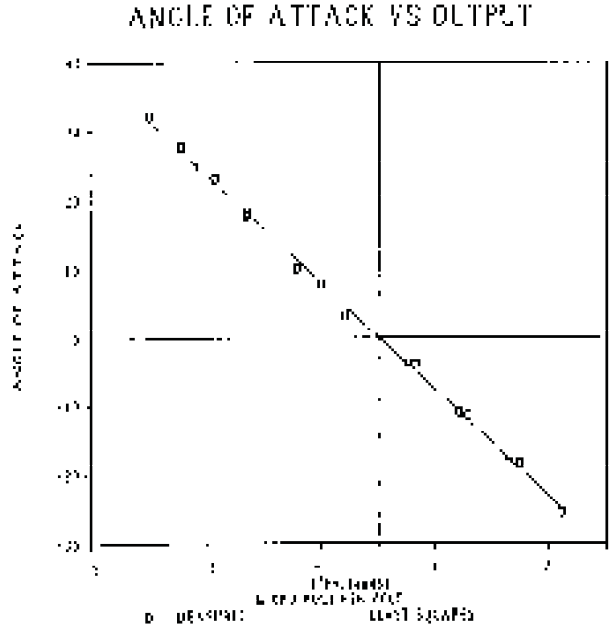


Fig. 6.32. Calibration of Attack transducer.

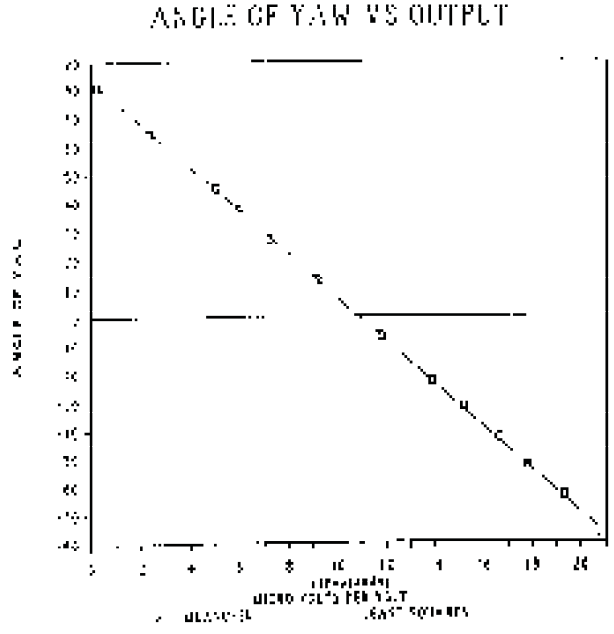


Fig. 6.33. Calibration of Yaw transducer.

$$ATTACK = -0.00775(V - V_0)$$

$$YAW = -0.00762(V - V_0)$$

The error in the yaw and attack calibration was very small as the least squares fit gave an R^2 value for the attack and yaw of 99.83 and 99.97 respectively.

7 RESULTS

7.1 VARIATION OF DRAG WITH REYNOLDS NUMBER

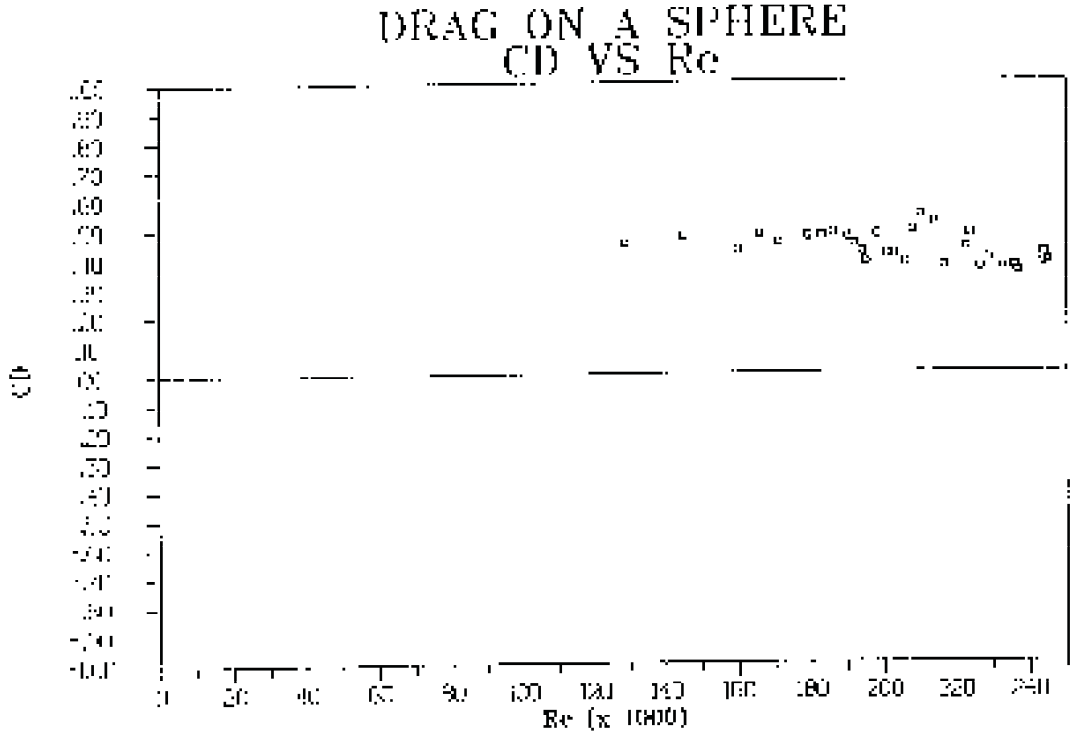


Fig 7.1. Drag on a stationary sphere using support A in position 1 with the sting parallel to the wind axis.

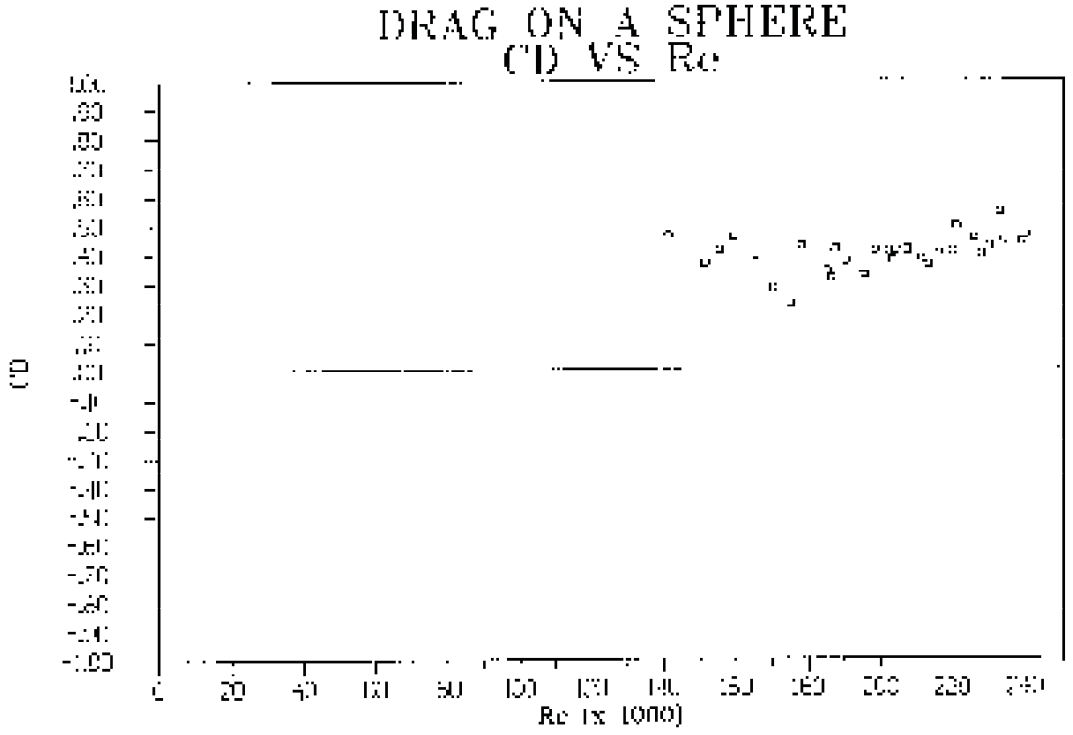


Fig 7.2. Drag on a stationary sphere using support A in position 1 with the sting perpendicular to the wind axis.

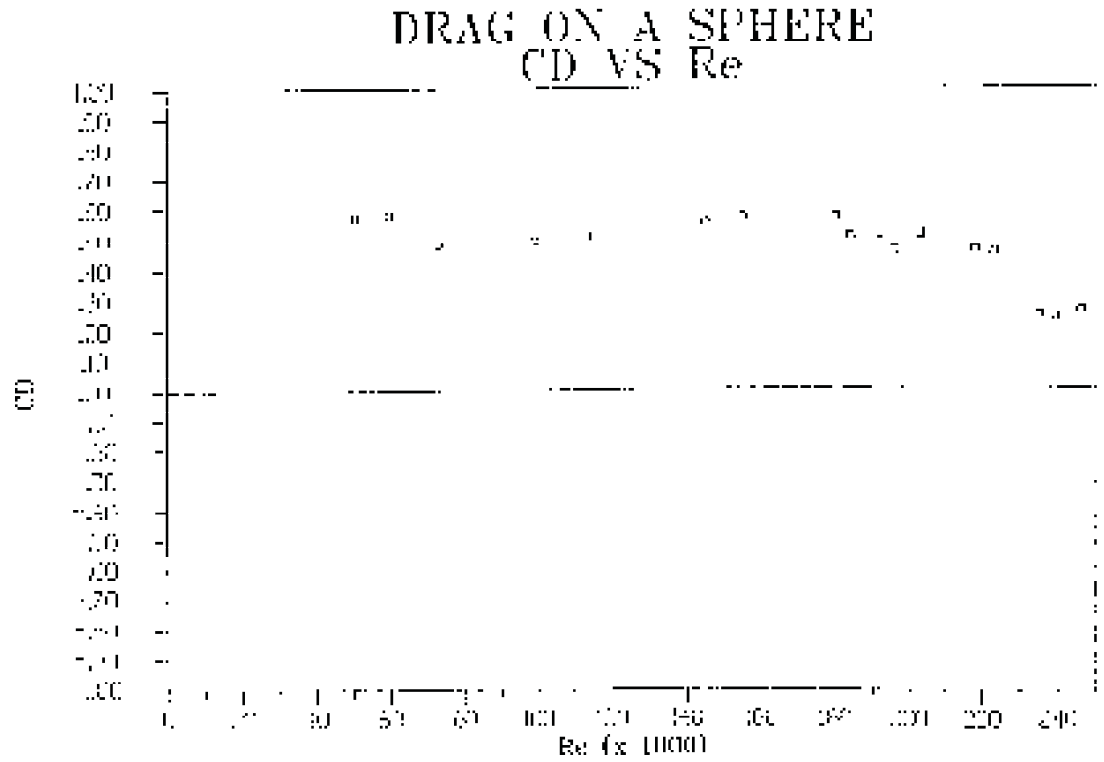


Fig 7.3. Drag on a stationary sphere using support A in position 1 with the support tied down.

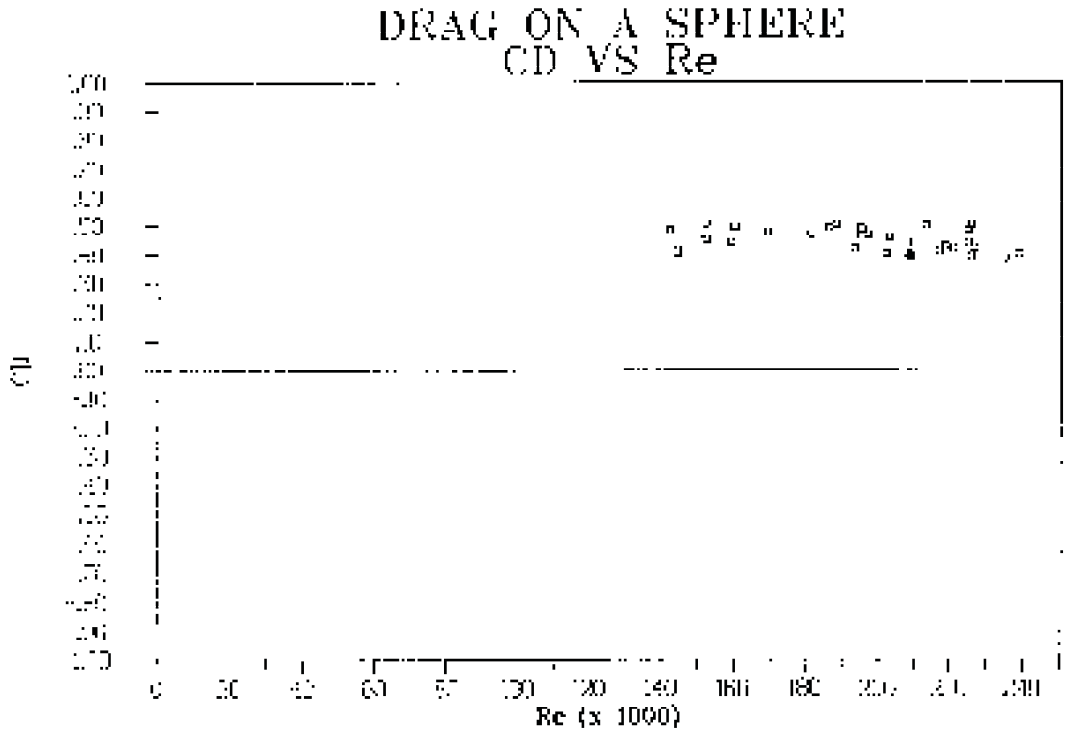


Fig 7.4. Drag on a stationary sphere using support B in position 2 with the spin axis parallel to the wind axis.

7.2 VARIATION OF LIFT WITH SPIN PARAMETER

All the figures below show the Lift generated when the sphere is rotated with the axis of spin perpendicular to the wind axis.

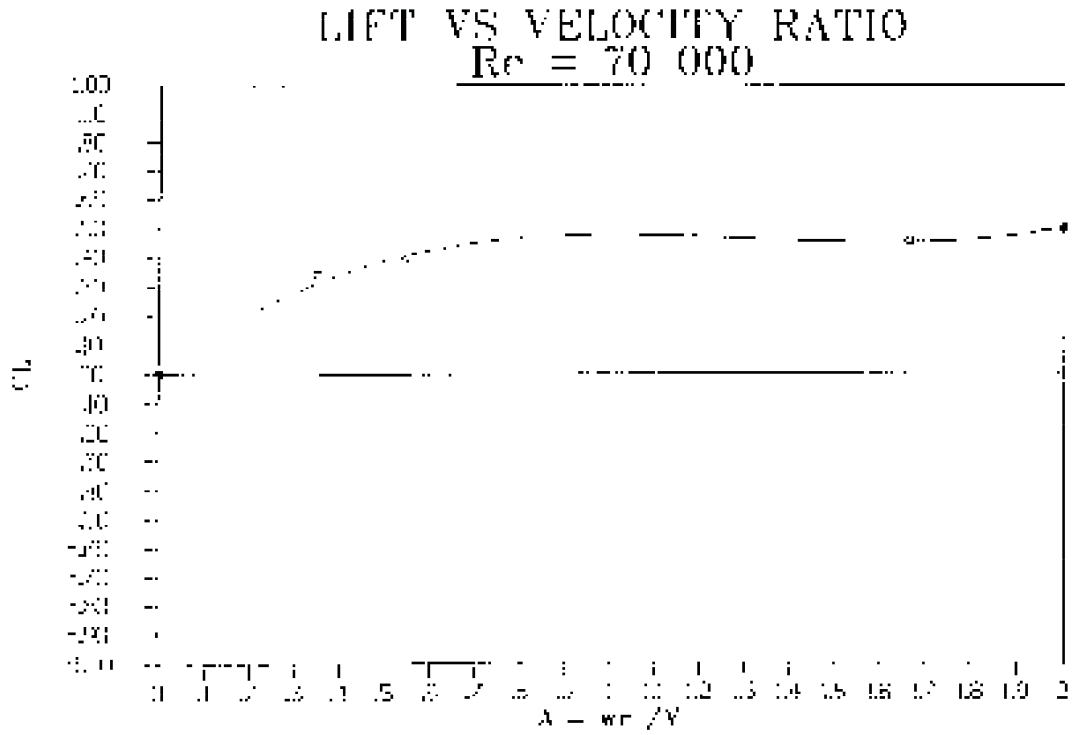


Fig 7.5. Lift vs velocity ratio for Re = 70 000 with $\gamma = 90°$ using support A in position 1.

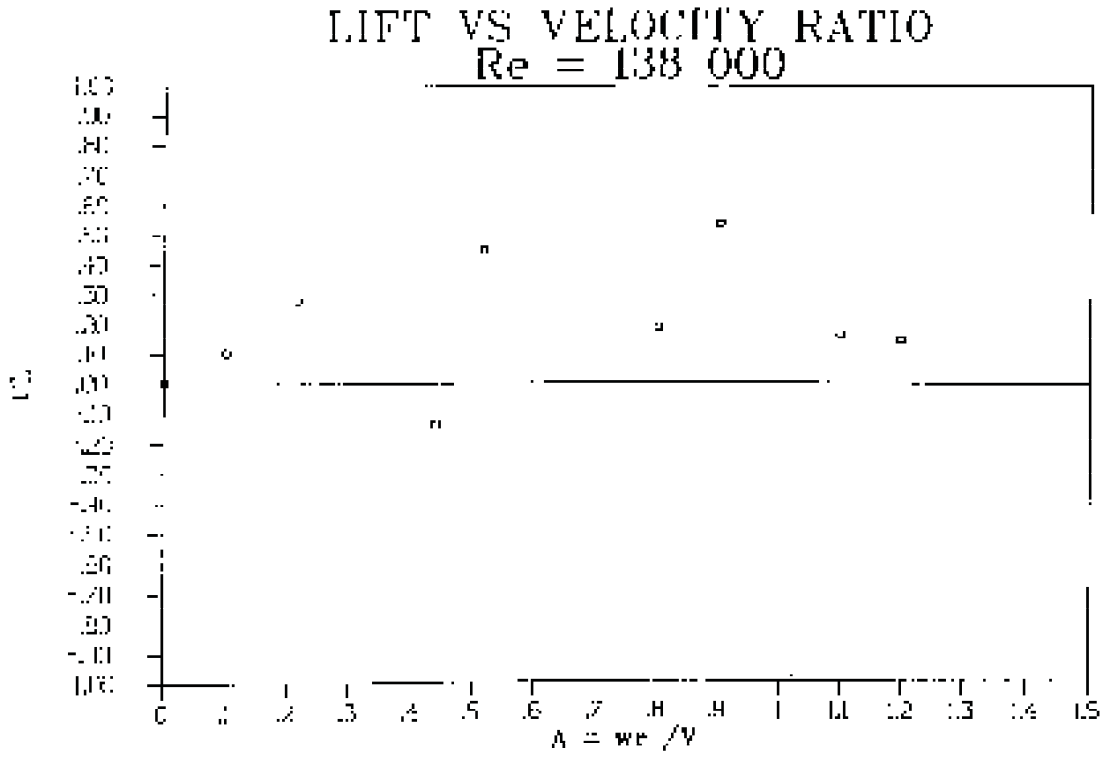


Fig 7.6. Lift vs velocity ratio for Re = 138 000 with $\gamma = 90°$ using support A in position 1.

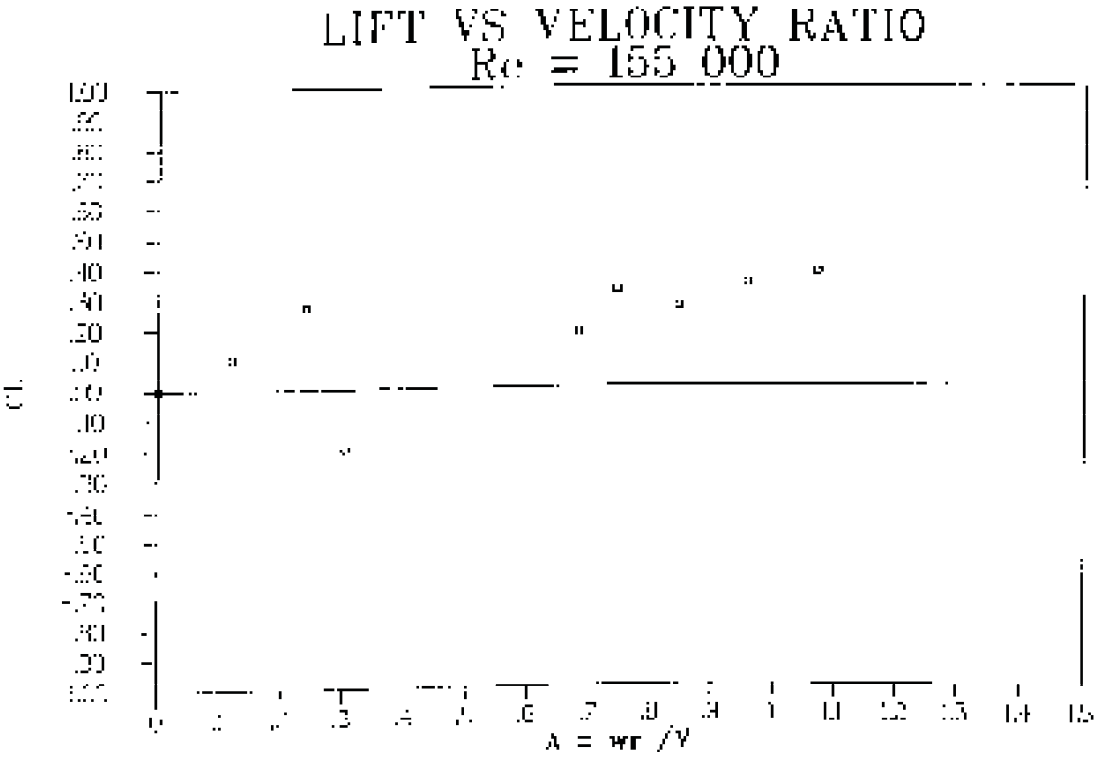


Fig 7.7. Lift vs velocity ratio for Re = 155 000 with $\gamma = 90°$ using support A in position 1.

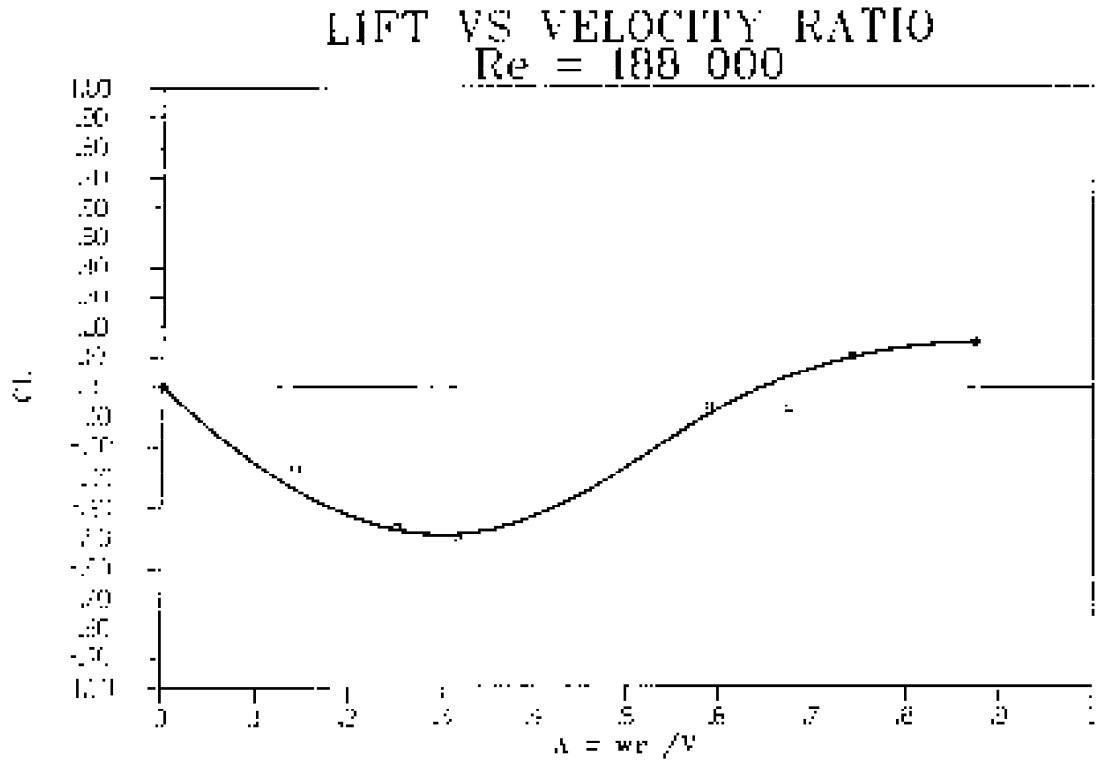


Fig 7.8. Lift vs velocity ratio for Re = 188 000 with $\gamma = 90°$ using support A in position 1.

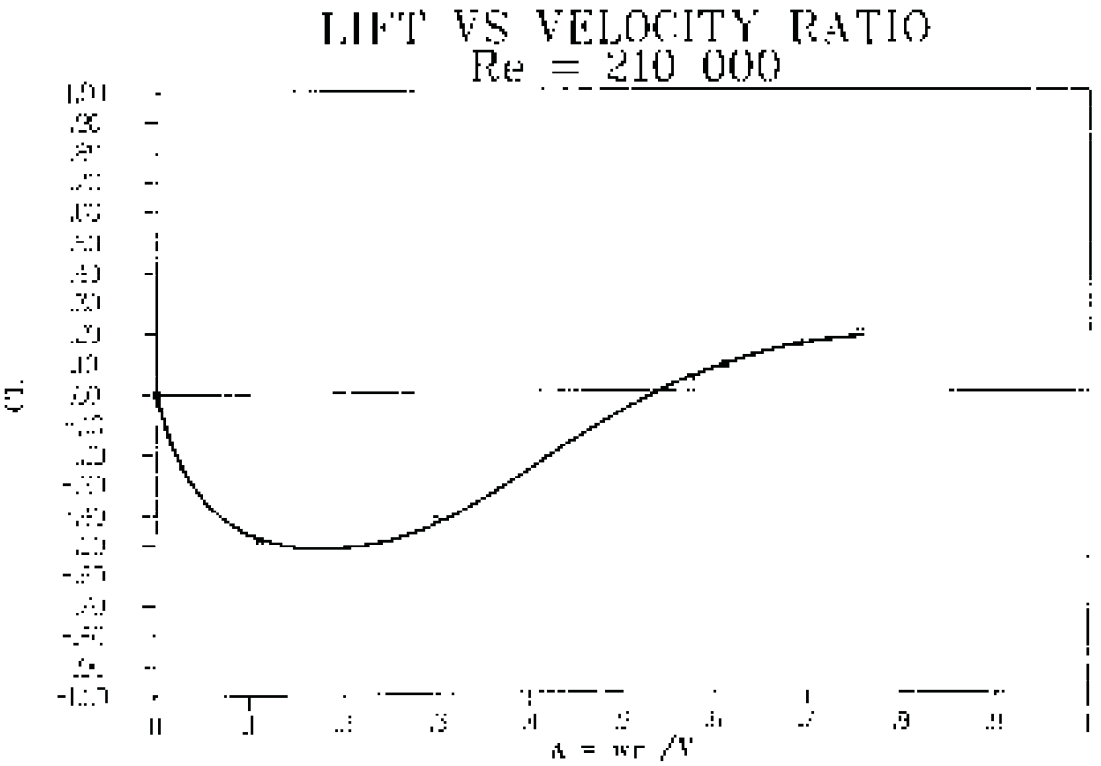


Fig 7.9. Lift vs velocity ratio for Re = 210 000 with $\gamma = 90°$ using support A in position 1.

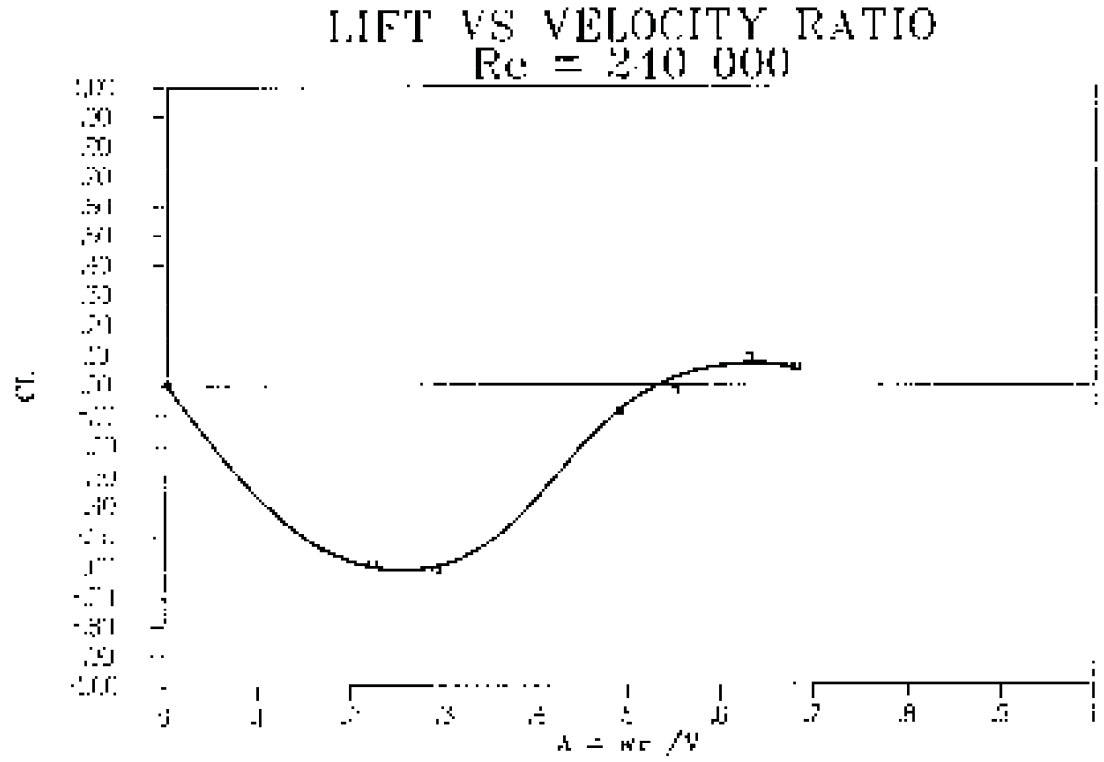


Fig 7.10. Lift vs velocity ratio for Re = 240 000 with γ = 90° using support A in position 1.

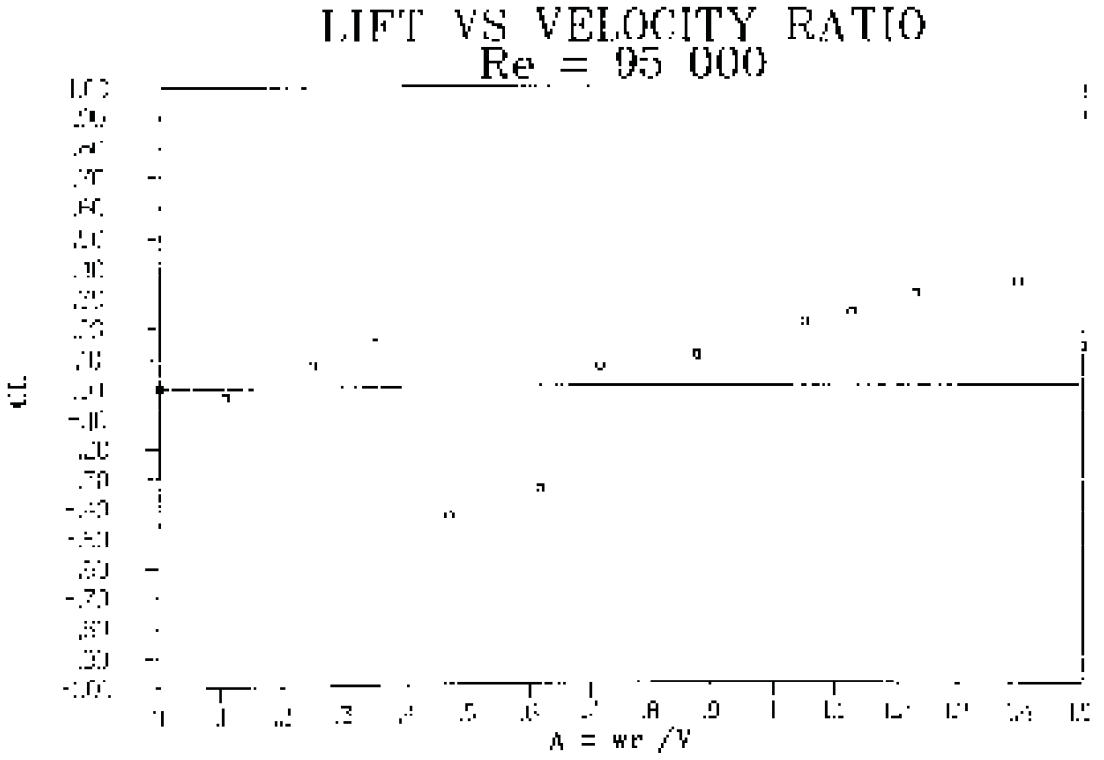


Fig 7.11. Lift vs velocity ratio for Re = 95 000 with γ = 90° using support A in position 2.

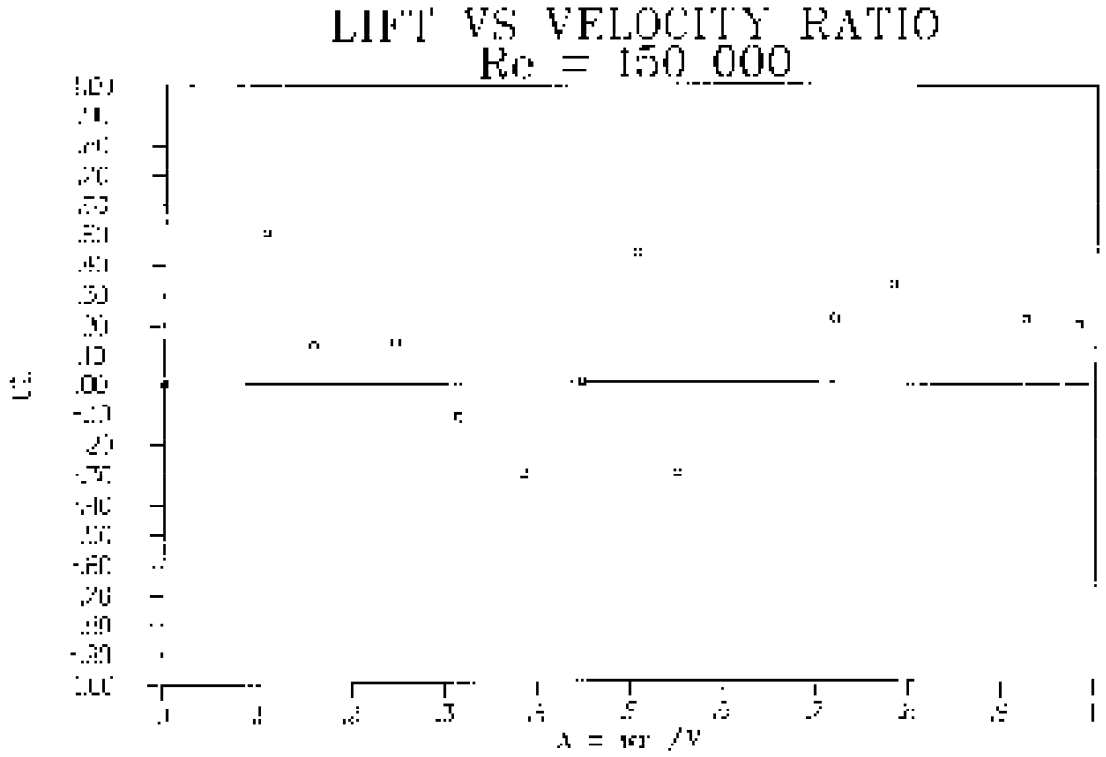


Fig 7.12. Lift vs velocity ratio for Re = 150 000 with γ = 90° using support A in position 2.

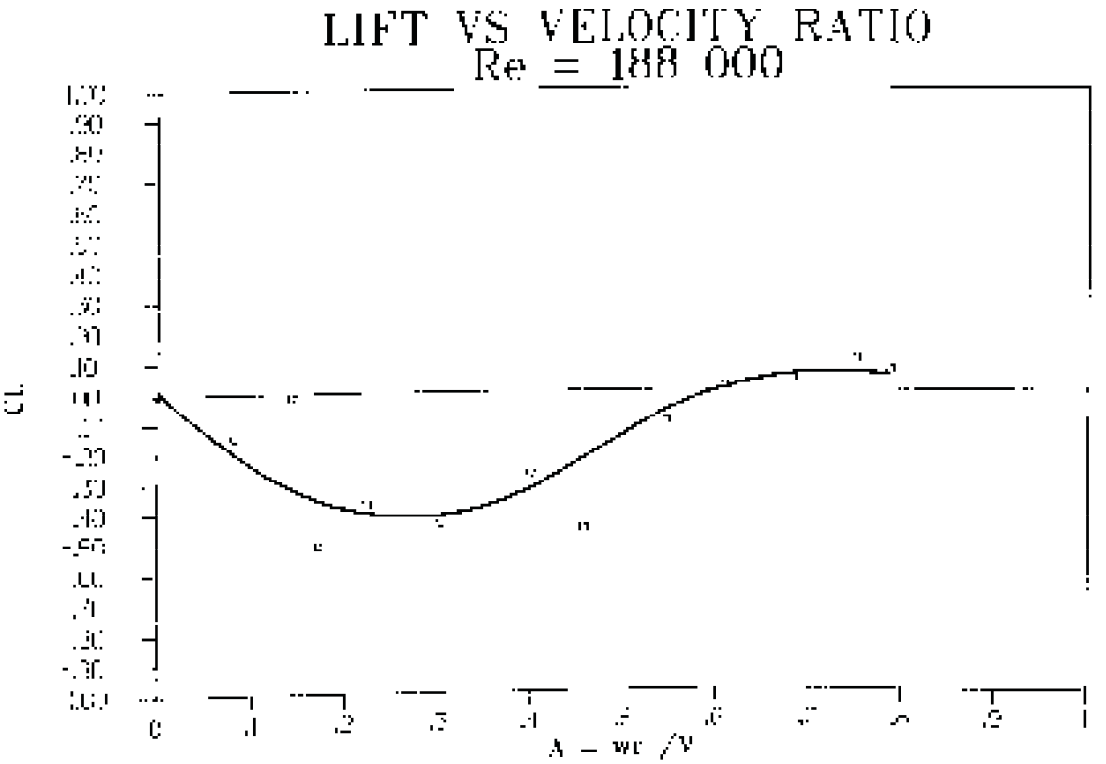


Fig 7.13. Lift vs velocity ratio for Re = 188 000 with γ = 90° using support A in position 2.

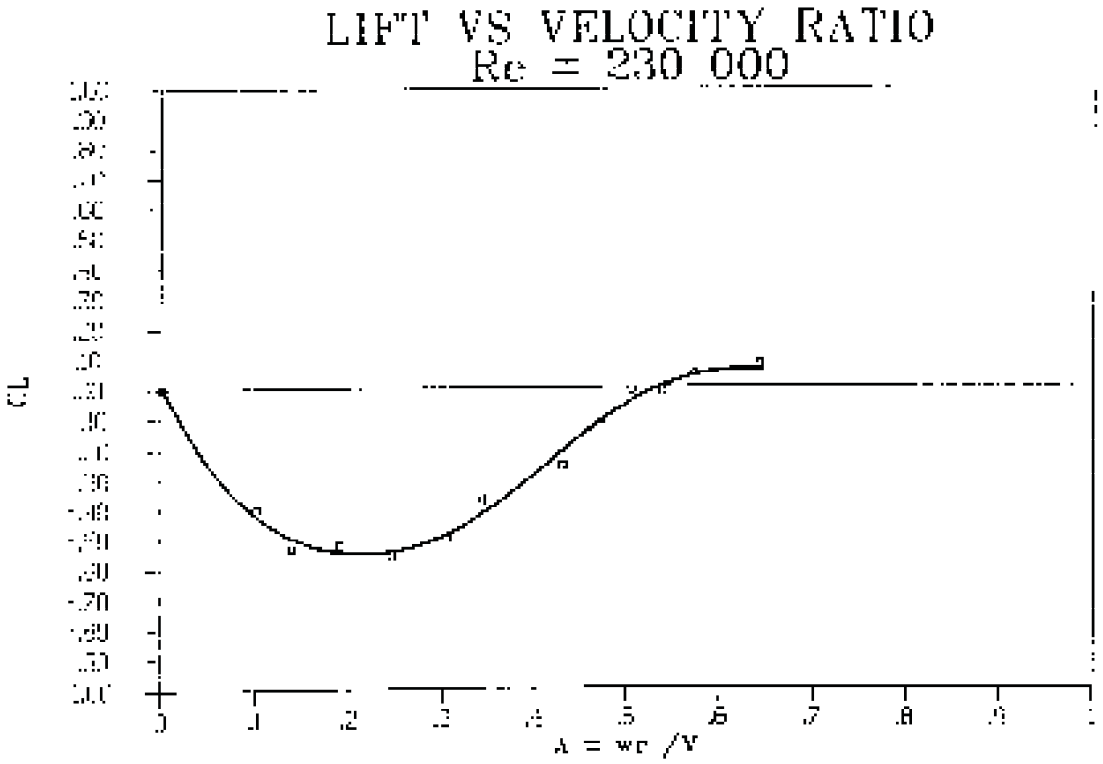


Fig 7.14. Lift vs velocity ratio for Re = 230 000 with $\gamma = 90°$ using support A in position 2.

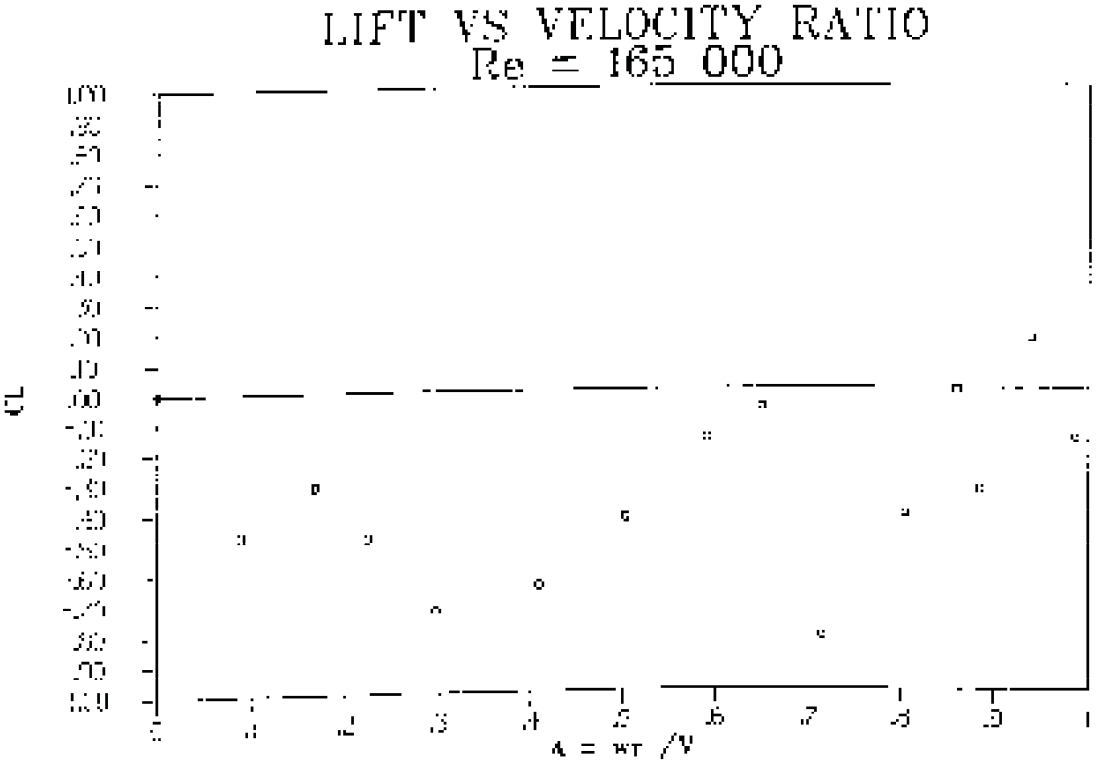


Fig 7.15. Lift vs velocity ratio for Re = 165 000 with $\gamma = 90°$ using support B in position 2.

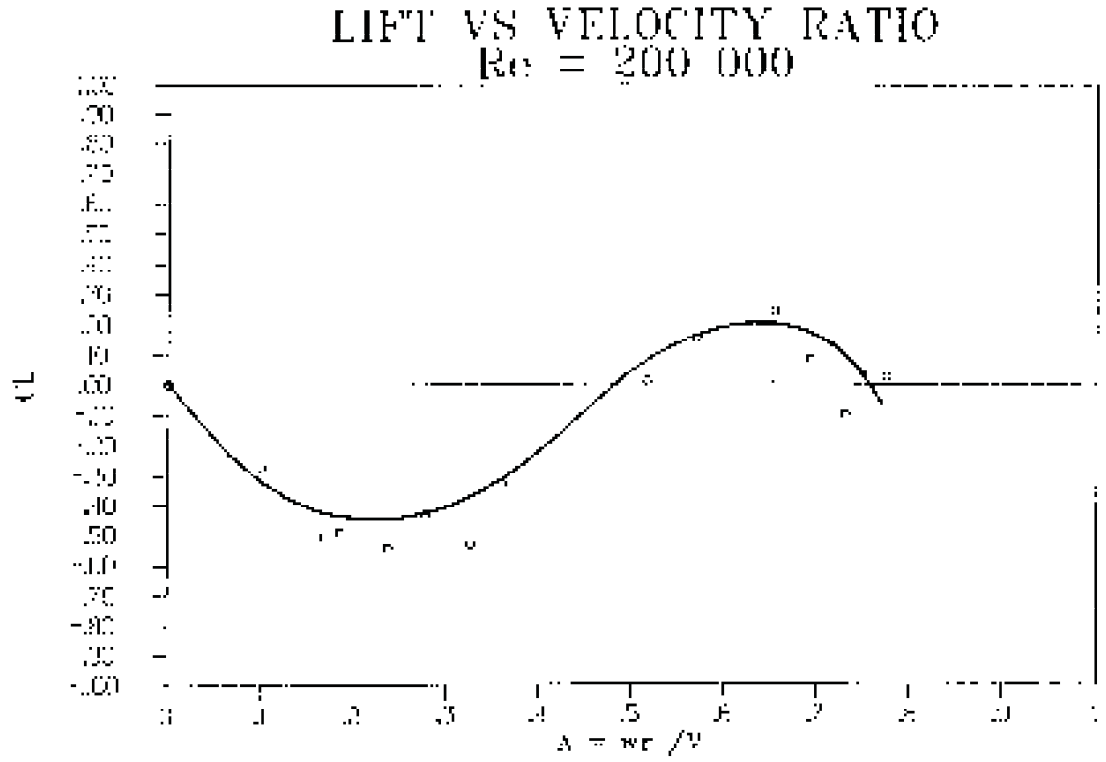


Fig 7.16. Lift vs velocity ratio for Re = 200 000 with $\gamma = 90°$ using support B in position 2.

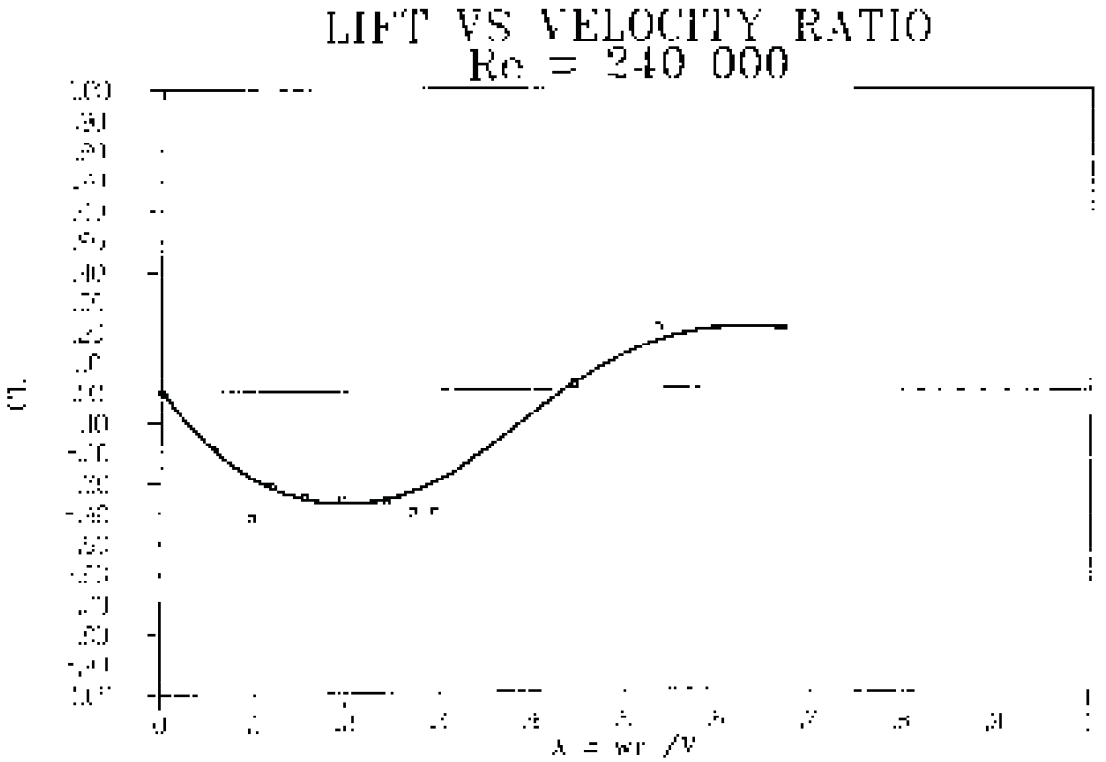


Fig 7.17. Lift vs velocity ratio for Re = 235 000 with $\gamma = 90°$ using support B in position 2.

The following three figures show the results of those tests using the same support and position on a common set of axes.

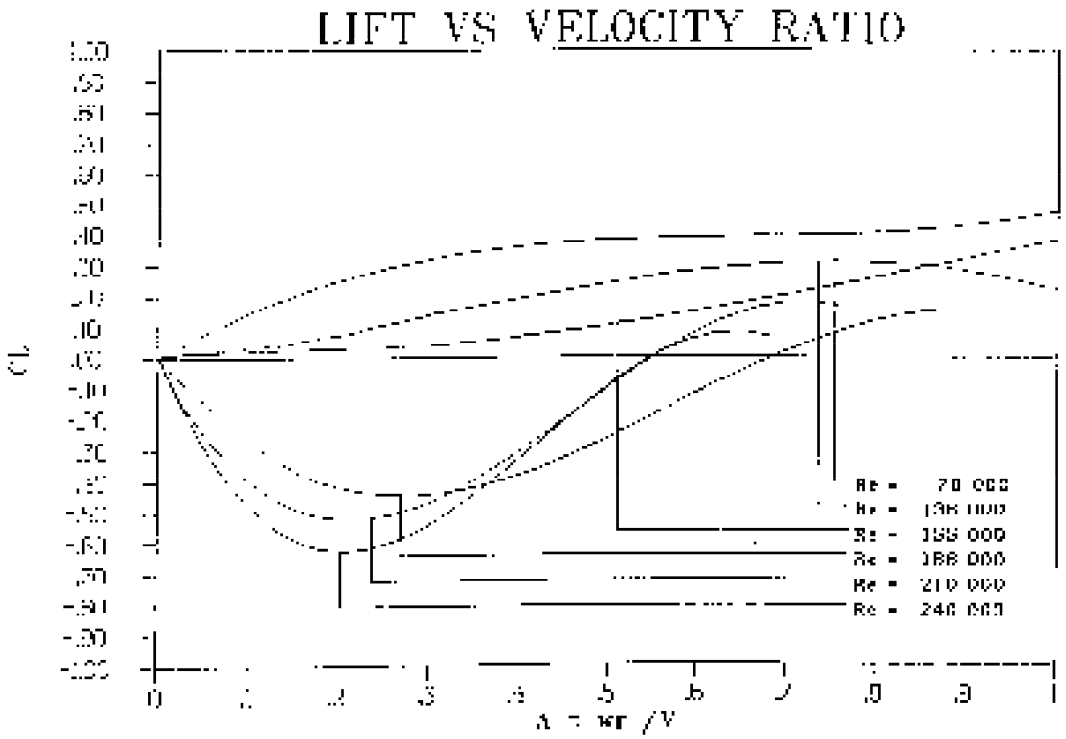


Fig 7.18. Lift vs velocity ratio with $\gamma = 90°$ for those tests using support A in position 1.